Journal of
Materials Chemistry A

PAPER

View Article Online
View Journal | View Issue

Cite this: *J. Mater. Chem. A*, 2019, **7**, 3924

Highly effective fabrication of two dimensional metal oxides as high performance lithium storage anodes†

Zhi Chen,‡[a] Cun Wang,‡[a] Min Chen,[a] Changchun Ye,[a] Zeheng Lin,[a] Lidan Xing,[ab] Youhao Liao,[ab] Mengqing Xu,[ab] Guozhong Cao *[c] and Weishan Li *[ab]

A facile strategy is proposed to control the morphology of manganese oxide (MnO), which is based on the ratio regulation of the solvents, *N*,*N*-dimethylformamide (DMF) and water, during nucleation and growth of the manganese oxalate precursor in solution. Various physical characterizations combined with theoretical calculations demonstrate that the crystal nucleation and growth of the precursor are highly dependent on the solvent composition, and thus the precursor as well as the resulting MnO can be controlled morphologically by regulating the ratio of water to DMF. Electrochemical measurements indicate that the sample with a two dimensional flake morphology exhibits excellent lithium storage performances in terms of specific capacity, cycling stability and rate capability, especially when carbon nanotubes (CNTs) are introduced during the precursor formation. The resulting composite of MnO and CNTs delivers a capacity of 1158 mA h g^{-1} after 300 cycles at 0.2 A g^{-1}. Even at 2 A g^{-1}, a remarkable capability of ~630 mA h g^{-1} is achieved. When the composite is paired with a high-nickel cathode (NCA) in a full cell, an energy density of 426 W h kg^{-1} is harvested, indicative of their potential applications in next-generation lithium ion batteries.

Received 1st December 2018
Accepted 20th January 2019

DOI: 10.1039/c8ta11555a

rsc.li/materials-a

1. Introduction

With the depletion of fossil fuels and the emergency due to environmental pollution, it becomes more and more necessary to develop new energy storage devices for efficient and clean exploitation of energy. Lithium ion batteries (LIB) as electrochemical energy storage devices have been widely used to power electric vehicles and portable electronics, owing to their high energy density, long lifespan and environmental benignity.[1–5] However, LIB with higher energy densities and a longer cycling life are still a big challenge for the incessant requirement.[6,7] The currently used anode in commercialized LIB is graphite, which provides a theoretical specific capacity of 372 mA h g^{-1}.[8–12] To increase the energy density of LIB, researchers are interested in substituting transition metal oxides (TMOs) for graphite owing to their three-fold theoretical specific capacity than that of graphite. Among the TMOs, MnO has been intensively studied because of its low operating potential (1.032 V *vs.* Li/Li^+) and low voltage hysteresis (<0.8 V) as well as its abundant resources and environmental benignity.[13–21]

It is well known that the structure and morphology of electrode materials greatly contribute to their electrochemical performance.[22–25] Consequently, much effort has been devoted towards fabricating hierarchical structures and specific morphologies of MnO.[21,25–27] Nevertheless, the strategies that have been proposed to date are complicated and difficult to apply on a large scale. In this study, we propose a facile scalable strategy to control the morphology of MnO, which involves a simple regulation of the organic-aqueous (*N*,*N*-dimethylformamide (DMF)–H_2O) solvent ratio for the crystal nucleation and growth of the MnC_2O_4 precursor. DMF as an organic solvent molecule participates in the crystallization in the form of a ligand,[28,29] affecting the length of the manganese oxalate chain and the size of the manganese oxalate crystal. Correspondingly, four manganese oxalate samples with various morphologies, including microrods (MR), two dimensional flakes (2D-F), microbars (MB), and irregular microparticles (IMP), were successfully synthesized by adjusting the H_2O/DMF volume ratio. After sintering, the MnO products inherited their precursor's morphology, except for the MR that turned into nanoparticles (NP) due to their longitudinal instability. Electrochemical tests demonstrated that the 2D-F exhibited

---

[a] *School of Chemistry and Environment, South China Normal University, Guangzhou 510631, China*

[b] *Engineering Research Center of MTEES (Ministry of Education), Research Center of BMET (Guangdong Province), Engineering Lab. of OFMHEB (Guangdong Province), Key Lab. of ETESPG (GHEI), and Innovative Platform for ITBMD (Guangzhou Municipality), South China Normal University, Guangzhou 510006, China. E-mail: liwsh@scnu.edu.cn*

[c] *Department of Materials Science and Engineering, University of Washington, Seattle, Washington 98195, USA. E-mail: gzcao@u.washington.edu*

† Electronic supplementary information (ESI) available. See DOI: 10.1039/c8ta11555a

‡ These authors contributed equally to this work.

excellent cycling stability and rate capability, especially when it was composited with carbon nanotubes (CNTs). An energy density of over 400 W h kg^{-1} was harvested when the resultant anode was paired with a high-nickel cathode (NCA) in a full cell, indicative of its potential application in next generation lithium ion batteries. To our knowledge, this is the first report on the control of the morphology and performances of manganese oxide anode by regulating the solvent ratios during the nucleation and growth of the manganese oxalate precursor in the solution. Most importantly, the mechanism of the morphological evolution has been explained by theoretical calculations.

2. Experimental section

2.1 Materials synthesis

Typically, 0.6329 g $H_2C_2O_4$ was dissolved in a mL DMF to obtain solution A (a = 50, 50, 50, 50, 40, 25, 10, and 0, respectively). Meanwhile, 0.245 g $Mn(CH_3COO)_2 \cdot 4H_2O$ was dissolved in b mL deionized water (b = 0, 0.5, 2.5, 5, 10, 25, 40, and 50, respectively) to obtain different concentrations of solution B. Subsequently, solution B was added dropwise into solution A, and the obtained mixed solution was stirred for 3 h. In these mixed solutions, the H_2O/DMF volume ratio was controlled to be 0 : 1, 1 : 100, 1 : 20, 1 : 10, 1 : 4, 1 : 1, 4 : 1, and 1 : 0, respectively. A white precipitate of the precursor, manganese oxalate, was collected and washed with absolute ethyl alcohol several times and finally dried at 60 °C for 4 h in a vacuum oven. MnO products were obtained by decomposing manganese oxalate under an argon atmosphere at 600 °C for 6 h with a heating rate of 2 °C min^{-1}.

CNTs were purchased from Cnano Technology. For purification, 0.4 g CNTs were dispersed in refluxing 200 mL 2 M HNO_3 for 6 h in a water bath at 60 °C to remove the impurities such as ash carbon or catalyst residues. They were then functionalized by 200 mL concentrated H_2SO_4/HNO_3 solution (3/1 volume ratio) in a water bath for 6 h at 60 °C and dried at 60 °C. For the fabrication of the 2D-F MnO/CNTs composite, as illustrated in Fig. S1,† 0.078 g CNTs after treatment were dispersed in 50 mL DMF, whereafter, 0.6329 g $H_2C_2O_4$ was dissolved in the above solution to obtain solution C. Meanwhile, 0.245 g $Mn(CH_3COO)_2 \cdot 4H_2O$ was dissolved in 0.5 mL deionized water to obtain solution D. Finally, solution D was added dropwise into solution C under constant stirring for 3 h. A black precipitate was collected by filtering the reaction mixture, washing several times with absolute ethyl alcohol and drying at 60 °C under vacuum. The 2D-F MnO/CNTs composite was obtained by decomposing manganese oxalate under an argon atmosphere at 600 °C for 6 h at a heating rate of 2 °C min^{-1}.

2.2 Physical characterizations and calculations

The morphology of samples was observed by field emission scanning electron microscopy (FESEM, ZEISS ULTRA 55, Japan) and transmission electron microscopy (TEM, JEOL JEM-2100HR). The crystal structures of the samples were analyzed by X-ray diffraction (XRD, Ultima IV X-Ray diffractometer, Rigaku, Japan) with Cu K_α radiation. The scanning range from 5 to 90° (2θ) at a step of 5° min^{-1} was executed. Raman spectra were collected on a confocal Raman microscope (Raman, WITec alpha 300R, Ulm, Germany) using an excitation laser at 532 nm. Thermogravimetric analysis (TGA, TGA 8000, PerkinElmer, America) was carried out from room temperature to 700 °C at a heating rate of 40 °C min^{-1} in air to determine the content of CNTs in the samples. Surface elemental analysis was conducted by X-ray photoelectron spectroscopy (XPS, Kratos Axis Ultra Dld, Japan). The specific surface area was obtained by Brunauer–Emmett–Teller analysis (BET, V-Sorb X800, Gold APP Instruments Corporation, China) at the temperature of liquid nitrogen (77 K). The theoretical calculations were carried out by the Gaussian 03 package. The structures were optimized using the B3LYP method combined with a 6-311++G(d,p) basis set. Frequency analyses were executed concurrently with the same basis set for the purpose of confirming each optimized stationary point and making zero point energy (ZPE) corrections. The enthalpies and Gibbs free energies were calculated at 298.2 K.

2.3 Electrochemical measurements

CR 2025 coin cells were assembled in an Ar-filled MBraun glove box for electrochemical measurements. The 2D-F MnO/CNTs or MnO electrodes were prepared by mixing 70 wt% of active material, 20 wt% of acetylene black and 10 wt% of polyvinylidene difluoride (PVDF) binder in *N*-methylpyrrolidone (NMP) solvent to form a homogeneous slurry, coating the slurry on a Cu sheet, and then drying in a vacuum oven at 120 °C for 12 h. The high-nickel cathode (NCA) for the full cell was made by mixing 80 wt% of active material (Ningbo Jinhe New materials Co., Ltd.), 10 wt% of acetylene black and 10 wt% of PVDF binder in NMP solvent to form a homogeneous slurry, which was coated on an Al sheet. Metallic lithium foil was used as the counter electrode in the half cell. Celgard 2400 served as a separator, and 1 M $LiPF_6$ in the mixed solvent of ethylene carbonate (EC), ethyl methyl carbonate (EMC) and diethyl carbonate (DEC) (EC : EMC : DEC = 3 : 5 : 2 in wt%) as the electrolyte. The charge and discharge tests were performed on a Land cell test system (Land CT2001A, China) in the potential range from 0.01 V to 3.0 V at 25 °C. Cyclic voltammetry was conducted on a Solartron-1470E Cell Test at 25 °C between 0.01 V and 3 V at a sweep rate of 0.2 mV s^{-1}.

3. Results and discussion

Eight samples of the precursor, manganese oxalate, were prepared in various H_2O/DMF volume ratios. As shown in Fig. S2,† the morphology of the precursor is highly dependent on the solvent ratio and can be divided into four groups, namely, microrods (MR), two dimension flakes (2D-F), microbars (MB), and irregular microparticles (IMP), as per the H_2O/DMF volume ratios of 0 : 1, 1 : 100 to 1 : 20, 1 : 10 to 1 : 1, and 4 : 1 to 1 : 0, respectively. The representative morphologies of the four precursors are presented in Fig. S3.†

When the resulting precursors were characterized with FTIR and XRD, it was found that the precursors contained various contents of solvents, H_2O and DMF. Fig. S4† shows the FTIR spectra of precursors with various H_2O/DMF volume ratios. As seen, three kinds of spectra can be identified. The first corresponds to the precursors obtained from the H_2O/DMF ratios of 0 : 1, 1 : 100, 1 : 20, 1 : 10, and 1 : 4. The second corresponds to the ratios of 1 : 1 and 4 : 1, and the last to that of 1 : 0. Two peaks arise at around 3587.5 cm^{-1} and 1689.6 cm^{-1} in the first kind of precursors, corresponding to H–C in H–C═O and C–N.[30,31] However, no such peaks were found in the other two kinds of precursor, suggesting that only the first kind of precursor contains DMF. There are three groups of XRD patterns (Fig. S5†) corresponding to the precursors identified by FTIR. Compared with the standard PDF cards of XRD, we confirm that the crystal structure in the second kind of precursors is monoclinic $MnC_2O_4 \cdot 2H_2O$ (the H_2O/DMF volume ratios of 1 : 1 and 4 : 1), while that in the last one is orthorhombic $MnC_2O_4 \cdot 2H_2O$ (the H_2O/DMF volume ratio of 1 : 0). There is no standard PDF card available for the XRD patterns of the first kind of precursors. Based on the composition of $MnC_2O_4 \cdot 2H_2O$, this kind of precursor possesses the chemical form of $MnC_2O_4 \cdot x\text{DMF} \cdot (2-x)H_2O$. Since the precursor formed in the aqueous solution takes an irregular morphology, the various morphologies of the precursors in Fig. S3† result from the effects of DMF.

To understand the effect of DMF on the precursor morphology, theoretical calculations were performed. The optimized geometric structure of the precursor nucleus and the corresponding formation energy are shown in Fig. S6,† which are based on the attack of $C_2O_4^{2-}$ on the coordinates of Mn^{2+} with two molecules of the solvents, DMF or H_2O. $MnC_2O_4 \cdot 2\text{DMF}$ has the lowest formation energy and $MnC_2O_4 \cdot 2H_2O$ has the highest one, suggesting that the preferential nucleation of the precursor is in the order of $MnC_2O_4 \cdot 2\text{DMF}$, $[Mn(H_2O)(\text{DMF})]C_2O_4$ and $MnC_2O_4 \cdot 2H_2O$. The optimized geometric structure of the precursor nucleus when it is attacked by another $C_2O_4^{2-}$ (Fig. S7†) suggests that the resulting nucleus combines with $C_2O_4^{2-}$ to form a chain structure,[32] while the corresponding formation energy in Fig. S7† indicates that the preference of this attack is in the order of $MnC_2O_4 \cdot 2H_2O$, $[Mn(H_2O)(\text{DMF})]C_2O_4$ and $MnC_2O_4 \cdot 2\text{DMF}$. Therefore, $MnC_2O_4 \cdot 2\text{DMF}$ is the easiest to nucleate but the hardest to grow. However, the condition of $MnC_2O_4 \cdot 2H_2O$ is contrary. In the solutions with more availability of water molecules, the nucleus chain gets longer and combines with more chains *via* the hydrogen bond of H_2O,[33] resulting in a 2 or 3-dimensional morphology. As shown in Fig. S3,† depending on the H_2O/DMF volume ratios, various particle sizes are obtained for MR (about 50 nm in diameter and 2 μm in length), 2D-F (about 50 nm in thickness, 1 μm in width and 2 μm in length), MB (about 1 μm in thickness, 1 μm in width and 10 μm in length), and IMP (about 10 μm in diameter).

The formation processes of the four representative MnO samples are illustrated in Fig. 1A. In the solution with only DMF, the H_2O/DMF volume ratio being 0 : 1, no H_2O is present in the chain, so the precursor crystal grows in one dimension on the *X*-axis, resulting in an MR morphology. When the H_2O/DMF volume ratio increases to the range between 1 : 100 and 1 : 20, the number of H_2O in the chain increases and are present on the surface of the *X*–*Y* axes. The chain on the *X*-axis combines with the other chains through formation of hydrogen bonds on the *Y*-axis. However, DMF on the *Z*-axis does not provide hydrogen bonds as in the case of H_2O and yields a large steric hindrance, which impedes the crystal growth on the *Z*-axis, resulting in a 2D-F morphology. When the H_2O/DMF volume ratio increases to the range between 1 : 10 and 1 : 1, the number of H_2O in the chain further increases and are present not only on the *Y*-axis but also on the *Z*-axis. The number of H_2O is larger on one axis than the other, resulting in different crystal growth rates on the *Y*- and *Z*-axes and hence the MB morphology. With a larger H_2O/DMF volume ratio, almost all the DMF in the chains are replaced by H_2O and the crystal growth rate on the *Y*- and *Z*-axis increases without a significant difference, resulting in an IMP morphology. All the manganese oxalate precursors are converted into MnO products after sintering. The products maintain the morphologies of their precursors, except for the MR that turn into nanoparticles (NP, about 50 nm in diameter) due to their longitudinal instability, as shown in Fig. 1B–E.

Four MnO samples were further characterized for their structure, surface area and electrochemical performance. The obtained results are presented in Fig. 2. As shown in Fig. 2A, all the samples are indexed to the face-centered cubic phase of MnO (JCPDS card: 07-0230), suggesting that they have the same crystal structure although their morphology is different. The main peaks at 34.9°, 40.5°, 58.7°, 70.2°, 73.8° and 87.8° could be assigned to the (111), (200), (220), (311), (222) and (400) reflections of cubic MnO, respectively.[34] No residues or contaminants have been detected in the four XRD patterns, indicating the high purity of the product. Fig. 2B presents the surface area of the four samples, which were obtained from their nitrogen adsorption–desorption isotherms (Fig. S8†). The significant difference in surface areas, 10.11 $m^2\ g^{-1}$, 6.00 $m^2\ g^{-1}$, 2.17 $m^2\ g^{-1}$, and 0.84 $m^2\ g^{-1}$, for NP, 2D-F, MB, and IMP, respectively, is attributed to the different particle sizes of the four samples with the smallest one for NP and the largest one for IMP (Fig. 2B).

Generally, the smaller particle size of an electrode material provides a better rate capability due to the shorter distance for lithium ion transportation in the material and the larger specific surface area. However, the 2D-F with a larger particle size shows a better rate capability than the NP, as well as better performances than the MB and IMP. As shown in Fig. 2C, the 2D-F sample delivers the largest rate capacity of 344 mA h g^{-1} even at 2 A g^{-1}, compared to those of 258, 242 and 242 mA h g^{-1} for NP, MB and IMP, respectively. Similarly, the 2D-F delivers the largest initial reversible capacity, 860 mA h g^{-1} at 0.05 A g^{-1}, compared to those of 653, 570 and 508 mA h g^{-1} for NP, MB and IMP, respectively (Fig. 2D), and exhibits the best cycling stability, maintaining a capacity of 825 mA h g^{-1} after 100 cycles at 0.2 A g^{-1}, compared to those of 605, 445 and 386 mA h g^{-1} for NP, MB and IMP, respectively (Fig. 2E). Apparently, 2D-F exhibits the best electrochemical performances among all the MnO products with various morphologies as the anode for lithium ion batteries.

All the four samples showed a similar voltammogram (Fig. S9†), suggesting that they have the same crystal structure

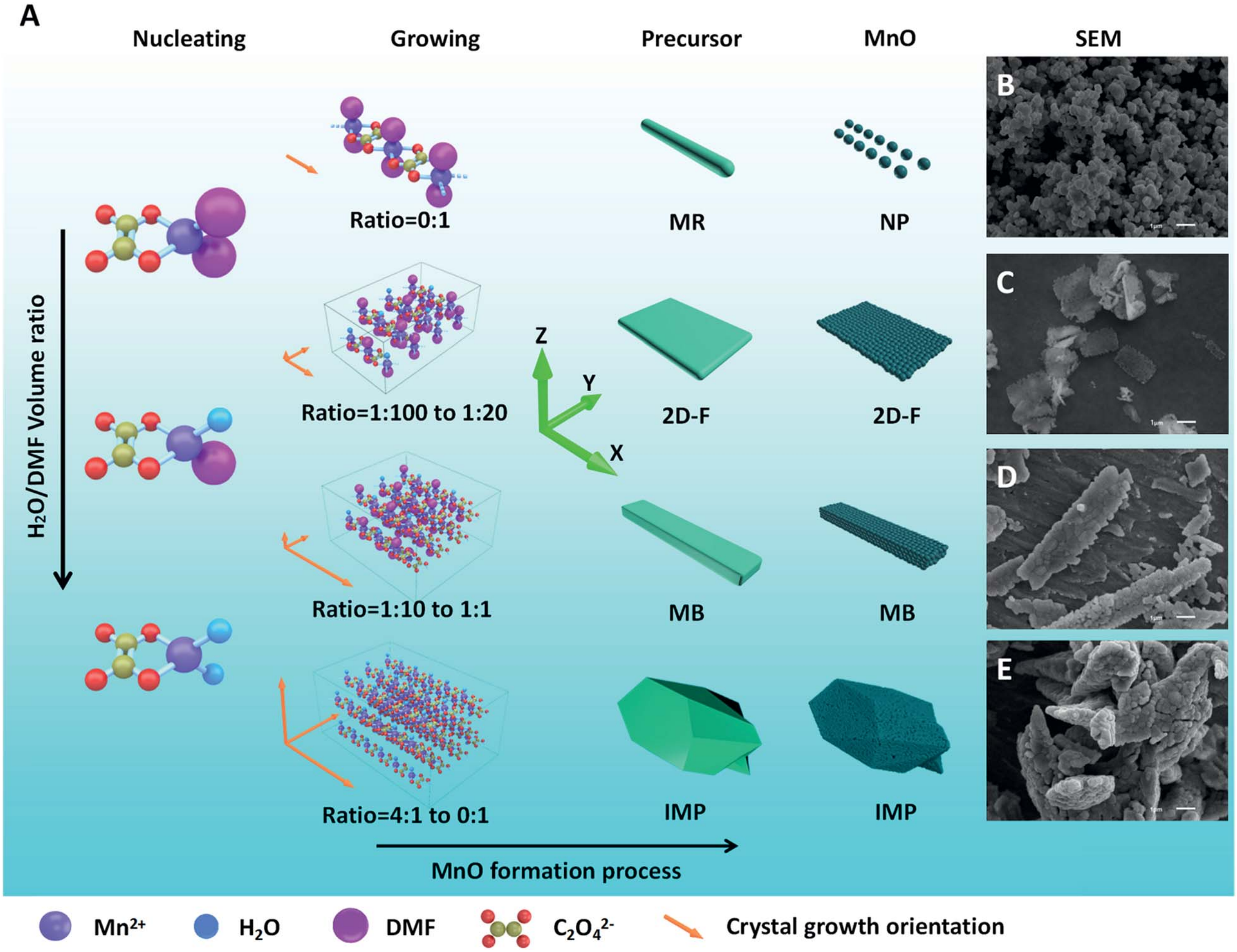

Fig. 1 Schematic illustration on the crystal nucleation and growth of precursors (A) and the resulting MnO that inherited their precursor's morphology; SEM images of MnO: NP (B), 2D-F (C), MB (D), and IMP (E).

and the difference in the electrochemical performances among the four samples resulted from their various morphologies. In their voltammograms, the reduction peak at around 0.66 V corresponds to the irreversible reduction of the electrolyte, which is accompanied by the formation of a solid electrolyte interphase (SEI) layer.[35–38] Besides, the reversible redox peaks at about 1.3 V for oxidation and 0.2 V for reduction can be seen.[27,39–43]

$$MnO + 2Li^+ + 2e^- = Mn + LiO_2 \tag{1}$$

The NP sample has the smallest particle size, which is beneficial for the rate capacity delivery due to the large specific surface area, the short distance in the solid-state bulk,[44,45] and the cycling stability maintenance due to the improved reversibility of the reaction (eqn (1)). The smaller the particle is, the more reversible the reaction is (eqn (1)). This is because the resulting Mn and Li_2O are closer and easily react to form MnO as the MnO becomes smaller. However, the smaller particle size also yields a negative effect: the electrolyte reduction decomposition takes place more actively and more SEI components accumulate on the MnO surface, which increases the interfacial impedance and mitigates the rate capability and cycling stability of MnO. The sample 2D-F has a flake morphology. This morphology provides not only a large surface area and a short distance for the reaction (eqn (1)), but also possesses dimensional stability due to inter-support among the sub-particles in the flake,[46,47] as illustrated in Fig. S10.† Compared with NP, 2D-F has a lower specific surface area and thus yields less SEI components, which can be confirmed by its higher initial coulombic efficiency (73%) than that of the NP (71%). With this unique feature, 2D-F exhibits better electrochemical performances than the NP (Fig. 2), in terms of specific capacity, cycling stability and rate capability. However, MB and IMP exhibit poorer performances than the NP and 2D-F due to their larger particle sizes.

To further improve the electrochemical performance of the 2D-F, CNTs were introduced into the solution for the formation of the 2D-F precursor and a new product, 2D-F MnO/CNTs, was obtained (Fig. S1†). Fig. 3 presents the morphological and structural characterizations of the resulting 2D-F MnO/CNTs. As shown in Fig. 3A, the introduction of the CNTs does not change the 2D flake morphology of MnO. Furthermore, the CNTs are uniformly embedded into the sub-particles of MnO (Fig. 3B).

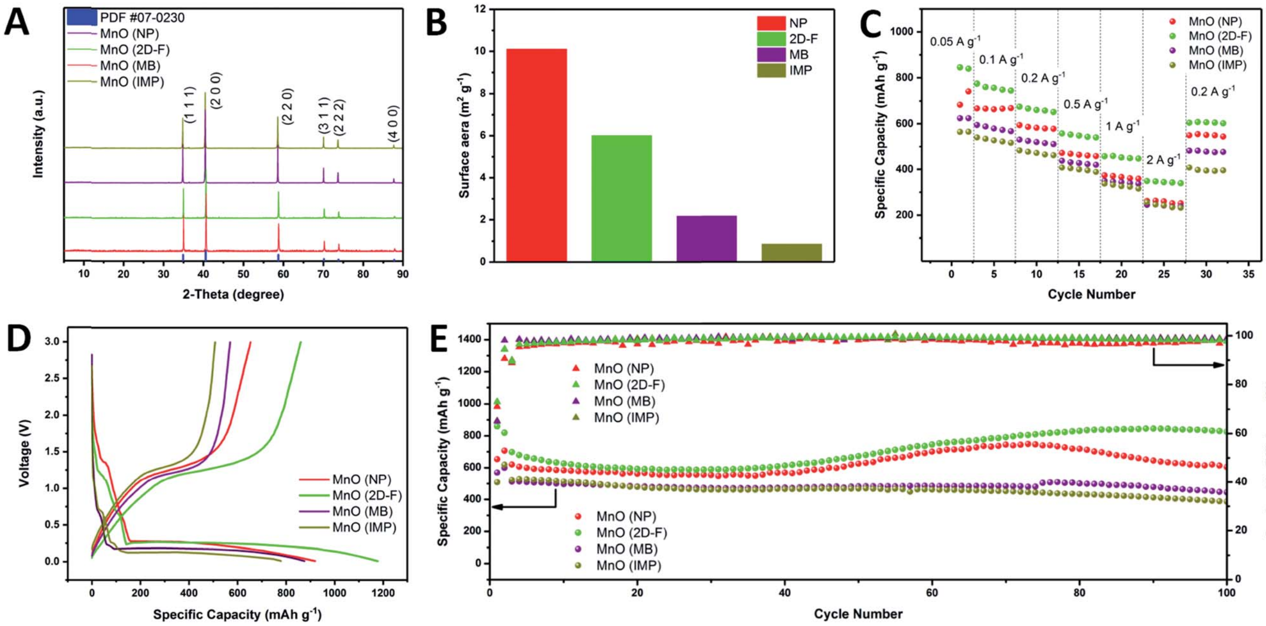

Fig. 2 XRD patterns (A), BET surface area (B), rate capability (C), initial discharge and charge profiles at 0.05 A g^{-1} (D), and cycling performance and coulombic efficiency at 0.2 A g^{-1} (E) for MnO samples with different morphologies.

The lattice fringe of MnO can be identified by HRTEM, with an interplanar distance of about 0.161 nm, attributed to the (220) plane of the cubic MnO (Fig. 3C). The elemental mappings (Fig. S11†) reveal the uniform distribution of C, O and Mn, substantiating that CNTs have been uniformly embedded into MnO.

Fig. 3D presents the TG curves of 2D-F, CNTs and 2D-F MnO/CNTs, which were obtained under an air flow condition with a heating rate of 40 °C min^{-1}. It can be found from Fig. 3D that the CNTs show a major weight loss due to its transformation to CO_2, while 2D-F has a weight increase due to the formation of manganese oxide with a higher valence from MnO. Based on these features, the content of CNTs in 2D-F MnO/CNTs is evaluated to be 6.6%. Fig. 3E displays the nitrogen adsorption and desorption isotherm of 2D-F MnO/CNTs, from which the specific surface area of 2D-F MnO/CNTs can be obtained. The specific surface area of 2D-F MnO/CNTs is 11.64 m^2 g^{-1}, which is larger than that of the 2D-F (6.00 m^2 g^{-1}), indicative of the

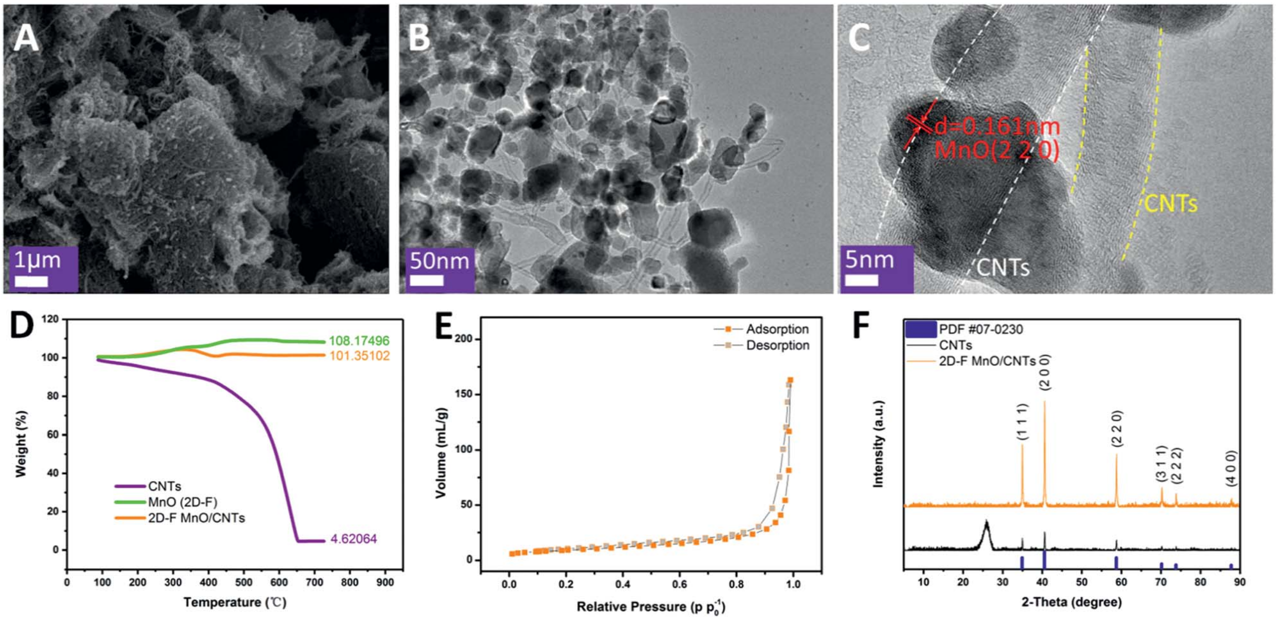

Fig. 3 SEM (A), TEM (B) and HRTEM (C) images of 2D-F MnO/CNTs. Thermogravimetric curves of 2D-F, CNTs and 2D-F MnO/CNTs (D). Nitrogen adsorption–desorption isotherm of 2D-F MnO/CNTs (E). XRD patterns of CNTs and 2D-F MnO/CNTs (F).

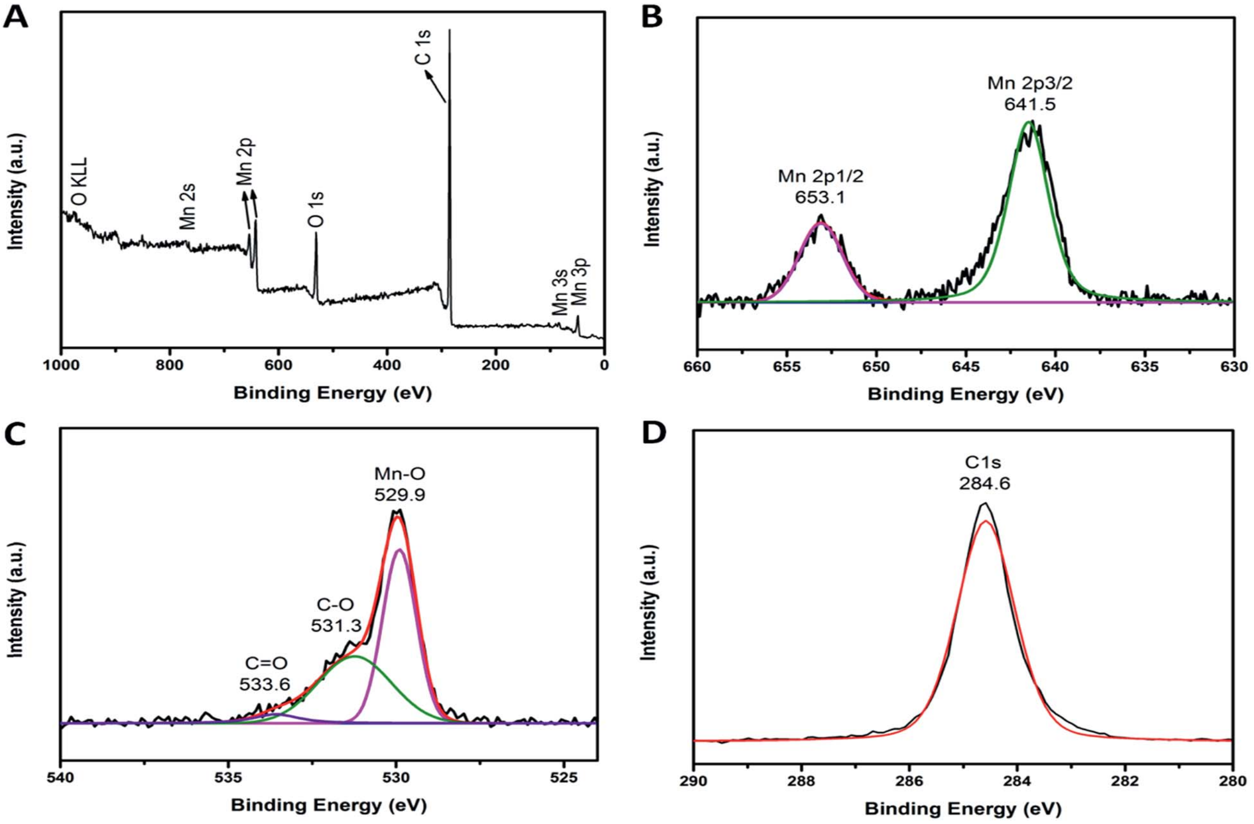

Fig. 4 XPS spectra for the 2D-F MnO/CNTs composite: the survey spectrum (A) and the high resolution spectra for Mn 2p (B), O 1s (C), C 1s (D).

contribution of CNTs (111.35 $m^2 g^{-1}$, as obtained from Fig. S12†). The XRD patterns (Fig. 3F) indicate that the introduction of CNTs does not change the crystal structure of MnO. The diffraction of CNTs cannot be observed in 2D-F MnO/CNTs due to its trace content and its far weaker diffraction than that of MnO.

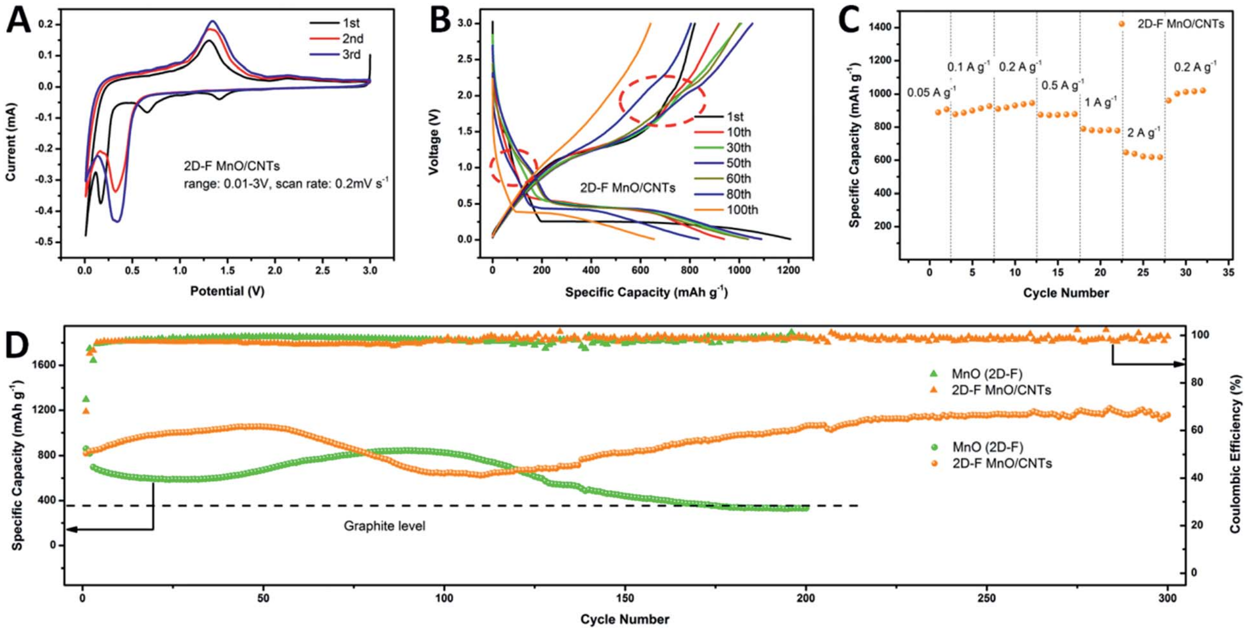

Fig. 5 CV curves for the first three cycles (A), discharge and charge profiles at 0.2 A g^{-1} between 0.01 and 3.00 V for the different cycles (B), rate capability (C), and cyclic stability at 0.2 A g^{-1} (D) for 2D-F MnO/CNTs.

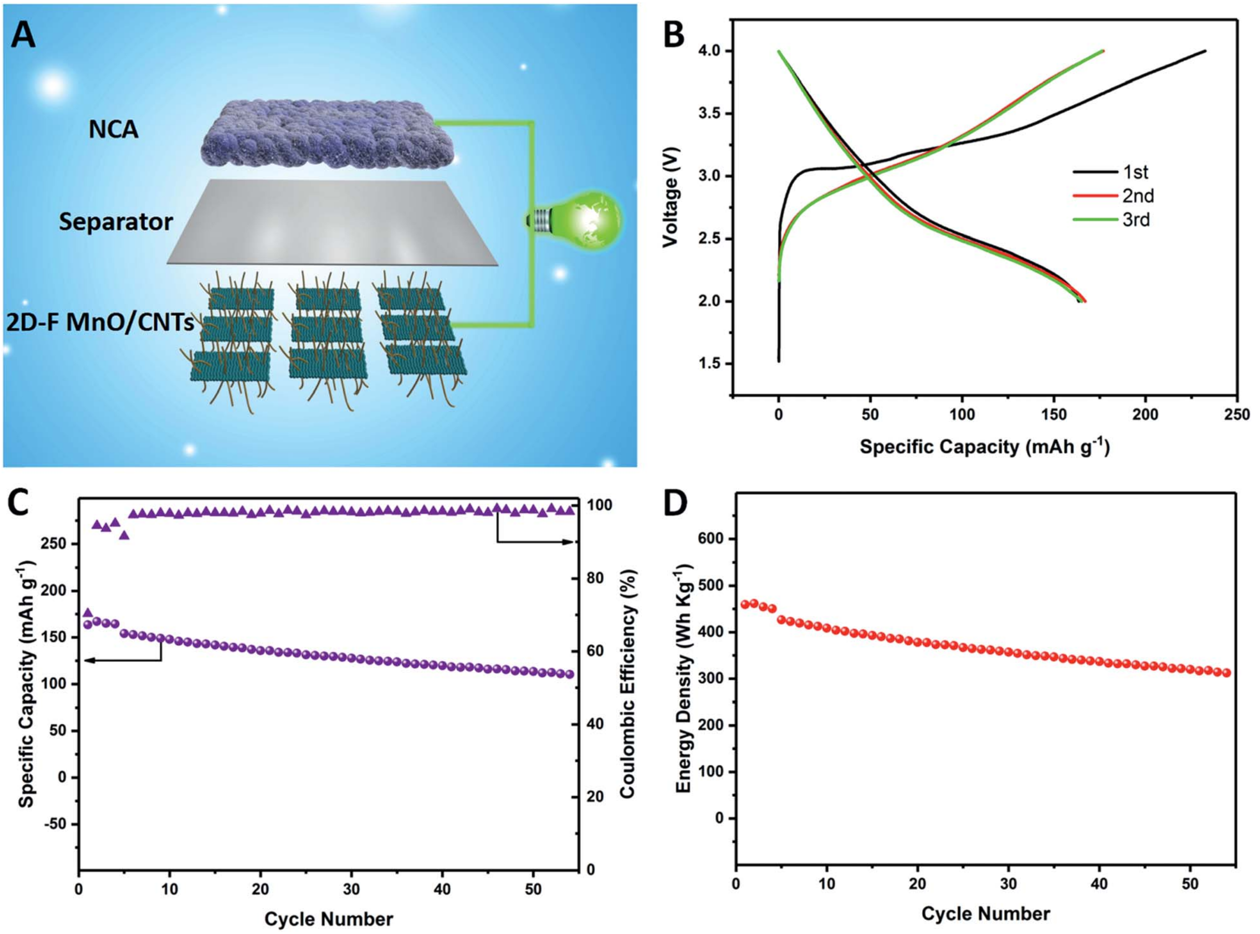

Fig. 6 Schematic illustration on NCA/2D-F MnO/CNTs full cell (A). Discharge/charge profiles at 0.3C (1C = 170 mA g^{-1}) between 2.00 V and 4.00 V (B), cycling performance and coulombic efficiency at 1C (C) and energy density (D) for NCA/2D-F MnO/CNTs full cell.

The surface electronic states of the elements in 2D-F MnO/CNTs were determined by XPS. The obtained results are presented in Fig. 4. As shown in Fig. 4A, the peaks for Mn (2s, 2p, 3s and 3p) and O (1s) can be associated to MnO, while the peak for C 1s stems from the CNTs. In Mn 2p spectra (Fig. 4B), the two main peaks located at 641.5 and 653.1 eV, corresponding to Mn(II) $2p_{3/2}$ and $2p_{1/2}$, respectively,[48–51] demonstrate that the manganese in 2D-F MnO/CNTs is in the form of Mn^{2+}. The peaks at 529.9, 531.3 and 533.6 eV in the O 1s spectra (Fig. 4C) correspond to the Mn–O, C–O and C═O, respectively.[25,52] The far stronger peak intensity of Mn–O than those of C–O and C═O suggests that the oxygen is mainly present in MnO and partially introduced from CNT in the forms of functional groups. In C 1s spectra (Fig. 4D), the strong peak located at 284.6 eV is assigned to the CNTs.[53,54] The Raman spectra (Fig. S13†) also verify the existence of MnO and CNTs in 2D-F MnO/CNTs, where the peak at around 647.2 cm^{-1} could be assigned to the Mn–O vibration,[13,34] while the broad peaks displayed at 1344.4 cm^{-1} and 1582.1 cm^{-1} are ascribed to the D and G bands of the CNTs.[47,55,56]

Fig. 5 presents the electrochemical performances of the resulting 2D-F MnO/CNTs. As shown in Fig. 5A, 2D-F MnO/CNTs show similar voltammetric behavior to that of MnO (Fig. S9†), suggesting that the introduction of CNTs into MnO does not change the lithiation/de-lithiation mechanism for MnO. However, the electrochemical performance of MnO significantly improved by the introduction of CNTs, as shown in Fig. 5B–D. At 2 A g^{-1}, the 2D-F MnO/CNTs delivered a specific capacity of 630 mA h g^{-1} (Fig. 5C), almost two times that of 2D-F MnO (344 mA h g^{-1}). Most importantly, the capacity delivered by 2D-F MnO/CNTs at 0.2 A g^{-1} reached 1100 mA h g^{-1} after 300 cycles (Fig. 5D). It can be noted from Fig. 5D that the capacity changed with the number of cycles in an "N" shape. During the initial 50 cycles, the capacity increased with the number of cycles, which can be ascribed to the contribution of the high valence manganese.[57,58] As indicated by the red circles in Fig. 5B, voltage plateaus at around 1.1 V and 2.0 V appear in the discharge/charge profile of 2D-F MnO/CNTs, which cannot be observed in that of 2D-F MnO (Fig. S14B†). Apparently, CNTs in 2D-F MnO/CNTs provide an electronically conductive network that facilitates the redox reactions involving manganese at various valencies besides Mn^{2+}.[17,52] From the 50th to the 100th cycle, the 2D-F MnO/CNTs suffered from capacity fading, which can be explained by the increased interfacial resistance due to the electrolyte decomposition.[44] After 100 cycles, the capacity gradually increased again and reached a maximum that is close to the theoretical specific capacity value of MnO_2. This feature can be explained by the reduction in the MnO particle size (Fig. S15†) due to the volume change under repeated lithiation/de-lithiation.[59,60] The MnO particles with reduced size provide more surface area for lithiation/de-lithiation, which is usually beneficial for capacity delivery. However, the particles with reduced size might lose their electronic contact, yielding an adverse impact on the capacity delivery. As shown in Fig. 5D, a fast capacity decay can be observed for 2D-F MnO after 100 cycles, which can be ascribed to the lost electronic contact among the MnO particles with reduced size, while a capacity value as high as the theoretical value of MnO_2 is maintained for 2D-F MnO/CNTs, which is indicative of the contribution of the CNTs. The CNTs in the 2D-F MnO/CNTs not only provide an electronically conductive network for MnO but also maintain the dimensional stability of MnO. These features can be confirmed by the far smaller impedance at all frequencies (Fig. S16†) and the corresponding smaller resistances (Table S1†) of the SEI film (R_f) and charge transfer resistance (R_{ct}) for 2D-F MnO/CNTs than those of the 2D-F MnO after various number of cycles. Consequently, 2D-F MnO/CNTs exhibit excellent electrochemical performances as an anode for the high energy density lithium ion battery. As shown in Table S2,† 2D-F MnO/CNTs produced by us exhibit better behaviour than the other MnO materials that have been reported in literature.

To demonstrate the possibilities for the resultant 2D-F MnO/CNTs in practical applications, a full cell was assembled using a pre-lithiated 2D-F MnO/CNTs anode and a high-nickel (NCA) cathode. The anode was pre-lithiated by pre-cycling 4 cycles in a half-cell. The obtained results are presented in Fig. 6, where the specific capacity and the energy density are given based on the cathode mass. It can be found from Fig. 6 that the resultant 2D-F MnO/CNTs anode works well when it is combined with the NCA cathode, suggesting that it is a promising anode for high energy density lithium ion batteries.

Conclusions

The volume ratio of solvents, *N*,*N*-dimethylformamide to water, has been demonstrated to significantly affect the morphology of the precursor manganese oxalate in a precipitation approach and the resultant MnO. This phenomenon determines the electrochemical performances of MnO as an anode for a high energy density battery. Based on this strategy, MnO products with various morphologies have been synthesized. It is found that MnO with a two dimensional flake morphology exhibited the best electrochemical performance, in terms of capacity delivery, rate capability and cycling stability. This result could be ascribed to its dimensional stability compared to that of MnO with nanoparticle size and its large surface area compared to that of bulky MnO samples. The electrochemical performances could be further improved by introducing carbon nanotubes (CNTs), which not only provided an electronically conductive network for MnO but also enforced the dimensional stability of MnO. The strategy established in this study provides a new route to facilely tune the morphology of the electrode materials for high-performance batteries, and is not limited to MnO.

Conflicts of interest

There are no conflicts to declare.

Acknowledgements

This study is financially supported by the National Natural Science Foundation of China (Grant No. 21872058), the National Key Research and Development Program of China (Grant No. 2018YFB0104000), and the Key Project of Science and Technology in Guangdong Province (Grant No. 2017A010106006).

Notes and references

1 M. Armand and J. M. Tarascon, *Nature*, 2008, **451**, 652–657.
2 J. Jiang, Y. Li, J. Liu, X. Huang, C. Yuan and X. W. Lou, *Adv. Mater.*, 2012, **24**, 5166–5180.
3 X. Zhang, Z. Xing, L. Wang, Y. Zhu, Q. Li, J. Liang, Y. Yu, T. Huang, K. Tang, Y. Qian and X. Shen, *J. Mater. Chem.*, 2012, **22**, 17864.
4 H. B. Lin, J. N. Hu, H. B. Rong, Y. M. Zhang, S. W. Mai, L. D. Xing, M. Q. Xu, X. P. Li and W. S. Li, *J. Mater. Chem. A*, 2014, **2**, 9272.
5 H. B. Lin, Y. M. Zhang, H. B. Rong, S. W. Mai, J. N. Hu, Y. H. Liao, L. D. Xing, M. Q. Xu, X. P. Li and W. S. Li, *J. Mater. Chem. A*, 2014, **2**, 11987.
6 W. Zhu, H. Huang, W. Zhang, X. Tao, Y. Gan, Y. Xia, H. Yang and X. Guo, *Electrochim. Acta*, 2015, **152**, 286–293.
7 S. Chen, P. Bao and G. Wang, *Nano Energy*, 2013, **2**, 425–434.
8 S.-Z. Huang, Y. Cai, J. Jin, J. Liu, Y. Li, Y. Yu, H.-E. Wang, L.-H. Chen and B.-L. Su, *Nano Energy*, 2015, **12**, 833–844.
9 Y. Zhao, X. Li, B. Yan, D. Xiong, D. Li, S. Lawes and X. Sun, *Adv. Energy Mater.*, 2016, **6**, 1502175.
10 D. Li, H. Wang, T. Zhou, W. Zhang, H. K. Liu and Z. Guo, *Adv. Energy Mater.*, 2017, **7**, 1700488.
11 K. Cao, T. Jin, L. Yang and L. Jiao, *Mater. Chem. Front.*, 2017, **1**, 2213–2242.
12 F. Wu, S. Zhang, B. Xi, Z. Feng, D. Sun, X. Ma, J. Zhang, J. Feng and S. Xiong, *Adv. Energy Mater.*, 2018, **8**, 1703242.
13 K. Zhang, P. Han, L. Gu, L. Zhang, Z. Liu, Q. Kong, C. Zhang, S. Dong, Z. Zhang, J. Yao, H. Xu, G. Cui and L. Chen, *ACS Appl. Mater. Interfaces*, 2012, **4**, 658–664.
14 Y. Sun, X. Hu, W. Luo and Y. Huang, *J. Mater. Chem.*, 2012, **22**, 19190.
15 B. Sun, Z. Chen, H.-S. Kim, H. Ahn and G. Wang, *J. Power Sources*, 2011, **196**, 3346–3349.
16 P.-C. J. C. Mao-Sung Wu, J.-T. Lee and J.-C. Lin, *J. Phys. Chem.*, 2005, **109**, 23279–23284.
17 Y. Sun, X. Hu, W. Luo, F. Xia and Y. Huang, *Adv. Funct. Mater.*, 2013, **23**, 2436–2444.
18 S. Guo, G. Lu, S. Qiu, J. Liu, X. Wang, C. He, H. Wei, X. Yan and Z. Guo, *Nano Energy*, 2014, **9**, 41–49.

19 J. Guo, Q. Liu, C. Wang and M. R. Zachariah, *Adv. Funct. Mater.*, 2012, **22**, 803–811.

20 S.-Y. Lee, L. Wu, A. S. Poyraz, J. Huang, A. C. Marschilok, K. J. Takeuchi, E. S. Takeuchi, M. Kim and Y. Zhu, *Adv. Mater.*, 2017, **29**, 1703186.

21 X. Gu, J. Yue, L. Chen, S. Liu, H. Xu, J. Yang, Y. Qian and X. Zhao, *J. Mater. Chem. A*, 2015, **3**, 1037–1041.

22 H. Su, Y. F. Xu, S. C. Feng, Z. G. Wu, X. P. Sun, C. H. Shen, J. Q. Wang, J. T. Li, L. Huang and S. G. Sun, *ACS Appl. Mater. Interfaces*, 2015, **7**, 8488–8494.

23 Y. Qiu, G.-L. Xu, K. Yan, H. Sun, J. Xiao, S. Yang, S.-G. Sun, L. Jin and H. Deng, *J. Mater. Chem.*, 2011, **21**, 6346.

24 M. Chen, Y. Zhang, L. Xing, Y. Liao, Y. Qiu, S. Yang and W. Li, *Adv. Mater.*, 2017, **29**, 201607015.

25 D. Sun, Y. Tang, D. Ye, J. Yan, H. Zhou and H. Wang, *ACS Appl. Mater. Interfaces*, 2017, **9**, 5254–5262.

26 Q. Sun, Z. Wang, Z. Zhang, Q. Yu, Y. Qu, J. Zhang, Y. Yu and B. Xiang, *ACS Appl. Mater. Interfaces*, 2016, **8**, 6303–6308.

27 S. Zhang, L. Zhu, H. Song, X. Chen and J. Zhou, *Nano Energy*, 2014, **10**, 172–180.

28 R. Mishra, M. Ahmad and M. R. Tripathi, *Polyhedron*, 2013, **54**, 189–195.

29 Y.-P. Zhao, H. Yang, F. Wang and Z.-Y. Du, *J. Mol. Struct.*, 2014, **1074**, 19–21.

30 G. G. Suchkova and L. I. Maklakov, *Vib. Spectrosc.*, 2009, **51**, 333–339.

31 M. Ferus, P. Kubelík and S. Civiš, *J. Phys. Chem. A*, 2011, **115**, 12132–12141.

32 N. Mancilla, V. Caliva, M. C. D'Antonio, A. C. González-Baró and E. J. Baran, *J. Raman Spectrosc.*, 2009, **40**, 915–920.

33 Z. A. D. Lethbridge, A. F. Congreve, E. Esslemont, A. M. Z. Slawin and P. Lightfoot, *J. Solid State Chem.*, 2003, **172**, 212–218.

34 Y. Xiao, X. Wang, W. Wang, D. Zhao and M. Cao, *ACS Appl. Mater. Interfaces*, 2014, **6**, 2051–2058.

35 K. Zhong, X. Xia, B. Zhang, H. Li, Z. Wang and L. Chen, *J. Power Sources*, 2010, **195**, 3300–3308.

36 Z. Cai, L. Xu, M. Yan, C. Han, L. He, K. M. Hercule, C. Niu, Z. Yuan, W. Xu, L. Qu, K. Zhao and L. Mai, *Nano Lett.*, 2015, **15**, 738–744.

37 F. Zheng, G. Xia, Y. Yang and Q. Chen, *Nanoscale*, 2015, **7**, 9637–9645.

38 J. Liu, N. Chen and Q. Pan, *J. Power Sources*, 2015, **299**, 265–272.

39 W.-M. Chen, L. Qie, Y. Shen, Y.-M. Sun, L.-X. Yuan, X.-L. Hu, W.-X. Zhang and Y.-H. Huang, *Nano Energy*, 2013, **2**, 412–418.

40 Y. H. Hao Jiang, S. Guo, C. Yan, P. S. Lee and C. Li, *ACS Nano*, 2014, **8**, 6308–6406.

41 J. Qin, Q. Zhang, Z. Cao, X. Li, C. Hu and B. Wei, *Nano Energy*, 2013, **2**, 733–741.

42 J. Yue, X. Gu, L. Chen, N. Wang, X. Jiang, H. Xu, J. Yang and Y. Qian, *J. Mater. Chem. A*, 2014, **2**, 17421–17426.

43 L. Zhang, G. Xia, Y. Huang, C. Wei, Y. Yu, D. Sun and X. Yu, *Energy Storage Materials*, 2018, **10**, 160–167.

44 Z. Cao, X. Chen, L. Xing, Y. Liao, M. Xu, X. Li, X. Liu and W. Li, *J. Power Sources*, 2018, **379**, 174–181.

45 H. B. Lin, H. B. Rong, W. Z. Huang, Y. H. Liao, L. D. Xing, M. Q. Xu, X. P. Li and W. S. Li, *J. Mater. Chem. A*, 2014, **2**, 14189.

46 J. Mei, T. Liao, L. Kou and Z. Sun, *Adv. Mater.*, 2017, **29**, 1700176.

47 Y. Xiao and M. Cao, *ACS Appl. Mater. Interfaces*, 2015, **7**, 12840–12849.

48 Z. X. Yang Xia, X. Dou, H. Huang, X. Lu, R. Yan, Y. Gan, W. Zhu, J. Tu, W. Zhang and X. Tao, *ACS Nano*, 2013, **7**, 7083–7092.

49 W. Luo, X. Hu, Y. Sun and Y. Huang, *ACS Appl. Mater. Interfaces*, 2013, **5**, 1997–2003.

50 P. Xia, H. B. Lin, W. Q. Tu, X. Q. Chen, X. Cai, X. W. Zheng, M. Q. Xu and W. S. Li, *Electrochim. Acta*, 2016, **198**, 66–76.

51 Y. Chu, L. Guo, B. Xi, Z. Feng, F. Wu, Y. Lin, J. Liu, D. Sun, J. Feng, Y. Qian and S. Xiong, *Adv. Mater.*, 2018, **30**, 1704244.

52 D.-H. Liu, H.-Y. Lü, X.-L. Wu, B.-H. Hou, F. Wan, S.-D. Bao, Q. Yan, H.-M. Xie and R.-S. Wang, *J. Mater. Chem. A*, 2015, **3**, 19738–19746.

53 N. G. Akalework, C.-J. Pan, W.-N. Su, J. Rick, M.-C. Tsai, J.-F. Lee, J.-M. Lin, L.-D. Tsai and B.-J. Hwang, *J. Mater. Chem.*, 2012, **22**, 20977.

54 T. I. T. Okpalugo, P. Papakonstantinou, H. Murphy, J. McLaughlin and N. M. D. Brown, *Carbon*, 2005, **43**, 153–161.

55 E. F. Antunes, A. O. Lobo, E. J. Corat and V. J. Trava-Airoldi, *Carbon*, 2007, **45**, 913–921.

56 Y. Chen, M. Wang, M. Tian, Y. Zhu, X. Wei, T. Jiang and S. Gao, *Nano Energy*, 2017, **42**, 314–321.

57 T. Yuan, Y. Jiang, W. Sun, B. Xiang, Y. Li, M. Yan, B. Xu and S. Dou, *Adv. Funct. Mater.*, 2016, **26**, 2198–2206.

58 S. Wang, Y. Xing, C. Xiao, H. Xu and S. Zhang, *J. Power Sources*, 2016, **307**, 11–16.

59 H. Sun, G. Xin, T. Hu, M. Yu, D. Shao, X. Sun and J. Lian, *Nat. Commun.*, 2014, **5**, 4526.

60 S.-H. Yu, S. H. Lee, D. J. Lee, Y.-E. Sung and T. Hyeon, *Small*, 2016, **12**, 2146–2172.